LAWRENCE
LIVERMORE
NATIONAL
LABORATORY

LLNL-JRNL-469533

A computational study of x-ray emission from high-Z x-ray sources on the National Ignition Facility laser

J. D. Colvin, K. B. Fournier, J. Kane, S. Langer, M. J. May, H. A. Scott

February 8, 2011

High Energy Density Physics

Disclaimer

February 10, 2011

A computational study of x-ray emission from high-Z x-ray sources on the National Ignition Facility laser

Jeffrey D. Colvin, Kevin B. Fournier, Jave Kane, Steven Langer, Mark J. May and Howard A. Scott

Lawrence Livermore National Laboratory, Livermore, CA 94551

ABSTRACT

We have begun to use 350-500 kJ of 1/3-micron laser light from the National Ignition Facility (NIF) laser to create millimeter-scale, bright multi-keV x-ray sources. In the first set of shots we achieved 15% -18% x-ray conversion efficiency into Xe M-shell (~1.5-2.5 keV), Ar K-shell (~3 keV) and Xe L-shell (~4-5.5 keV) emission (Fournier *et al*., Phys. Plasmas 17, 082701, 2010), in good agreement with the emission modeled using a 2D radiation-hydrodynamics code incorporating a modern Detailed Configuration Accounting atomic model in non-LTE (Colvin *et al*., Phys. Plasmas, 17, 073111, 2010). In this paper we first briefly review details of the computational model and comparisons of the simulations with the Ar/Xe NIF data. We then discuss a computational study showing sensitivity of the x-ray emission to various beam illumination details (beam configuration, pointing, peak power, pulse shape, etc.) and target parameters (size, initial density, etc.), and finally make some predictions of how the x-ray conversion efficiency expected from NIF shots scales with atomic number of the emitting plasma.

1. Introduction and background

In this paper we report on our use of a new non-LTE atomic model incorporated into a 2D radiation-hydrodynamics computer code to match x-ray emission data from targets heated by the National Ignition Facility laser, and to predict scaling of x-ray emission with laser power and atomic number.

It has been known for some time that it may be feasible to create a bright, high-photon-energy x-ray source by heating a low-density target (like a gas or a metal-doped foam target having a density <0.1% of solid density) with a high-power laser [1]. Laser light of wavelength λ_L will propagate through any plasma that has an electron density less than the critical electron density, $n_c = 1.1 \times 10^{21}/\lambda_L(\mu m)^2$ cm^{-3}. Thus, for a frequency-tripled Nd-doped glass laser, like the NIF laser [2], with λ_L =1/3 μm, $n_c \tilde{=} 10^{22}$ cm^{-3}. For moderate laser intensities (~10^{14} – 10^{16} W cm^{-2}) the laser beam partially ionizes the material via multi-photon photo-ionization. Then, once free electrons are present, the laser deposits its energy along the beam path via inverse bremsstrahlung interactions with these free electrons. At sub-critical densities, the ionization wave and heating wave travel faster than the plasma sonic velocity [3]. Thus, the laser beam supersonically and volumetrically heats the low-density material on a time scale shorter than the time scale for the rarefaction wave to decompress and cool the plasma, providing much higher x-ray conversion efficiency (XRCE) in the non-LTE plasma than is obtained by simply irradiating solid targets [4,5,6]. Under-dense high-Z radiators have been confined in the past mainly to high-Z noble gases (Ar, Kr, and Xe) [7,8,9], but some efficient Ti x-ray sources (K-shell emission ~ 4 keV) have also been created with nano-fiber targets [10]; with pre-pulsed Ti, Cu, and Ge foils (K-shell emission ~ 4 keV, ~8 keV, and ~10 keV respectively) [11,12]; and by irradiating the inside surface of Ti-and Ge-lined cans [13,14].

Advances in non-LTE physics and the creation of efficient high-photon-energy x-ray sources have been enabled by three parallel developments in recent years: target

fabrication developments, the commissioning of higher-power lasers, and developments in modeling.

Target fabrication developments in metal-doped foams and pure metal foams have enabled the creation and characterization of larger-scale bright x-ray sources at various photon energies, particularly bright K-shell emitters in the ~3-13 keV photon energy range (between Ar and Kr). A wet chemical process has been developed to fabricate high-Z doped SiO_2 aerogel foams [15] and fashion them into laser targets. So far, the chemistry has been worked out for doping with Ti, Fe, Zn and Ge. In recent years experiments have been carried out on Ti-doped aerogel foams [16], and on Ge-doped aerogel foams [17], with comparable numbers of emitting ions as in gas targets.

Two additional target fabrication developments are currently underway. One of these is an atomic layer deposition (ALD) process in which high-Z atoms, like Ru, are deposited on the strands of carbon aerogel foam [18]. In another development, fabrication of pure-metal foams has begun. A novel four-step nano-synthesis technique for making ultra-low-density pure metal foams, based on ion lithography, was first proposed by Colvin and Felter [19]. This process produces a self-supporting array of nano-wires that have a thickness comparable to the skin depth of the laser light, ~10 nm. This is about one-tenth the diameter of the nano-fiber targets [10], which are made by electro-spinning of titanium-oxide-doped cotton fibers, and which have been made into laser targets. Simulations suggest that the pure metal nano-wire foam will heat volumetrically and homogenize in 100-200 ps. Neither the ALD foams nor the nano-wire foams have yet been fashioned into laser targets. Their development, though, promises a path to bright x-ray sources at even higher photon energies.

The commissioning of the NIF laser at the Lawrence Livermore National Laboratory has enabled the creation of larger, brighter, and higher-photon-energy K-shell emitters. NIF, a 192=beam laser system, is capable of delivering up to ~2 MJ of ultraviolet light (351 nm) to millimeter-scale targets at the center of a 10-m-diameter target chamber [2].

Five NIF experiments were conducted in October and November 2009 on Ar/Xe gas targets. Details of the experiments, the diagnostics, and the data have been given by Fournier *et al*. [20].

Development of a new super-configuration non-LTE atomic model and its incorporation into a 2D radiation-hydrodynamics computer code has enabled affordable integrated design and modeling of laser-driven x-ray sources. One key feature of the new model is that ionization states are calculated in the non-LTE conditions from a detailed super-configuration atomic model (DCA) [21]. Another key feature of the new model is that electron thermal conduction is treated in the Spitzer-Harm formulation [22] with a large flux limiter, f=0.2, which provides for more non-local heat transport. More details of this model, its implementation into the 2D radiation-hydrodynamics code Lasnex [23], and its benchmarking with the data from the Omega experiments on Ge-doped aerogel foams [17], is given in Reference 3. In this paper we discuss the application of this new modeling to the 2009 NIF Ar/Xe x-ray source experiments.

In the next section we discuss the results of the simulations of the NIF Ar/Xe x-ray source experiments and compare the simulated emissivities to the measured ones. In Section 3 we discuss what simulations with the new model predict for what we can expect as we scale up in laser power and in atomic number. Discussion and concluding summary are presented in Section 4.

2. Simulations and comparison with NIF data

Five NIF experiments were conducted in October and November 2009 on Ar/Xe targets. The targets consisted of a 65/35 Ar/Xe gas mix at 1.2 atm initial gas fill pressure (initial density 3.515 mg cm^{-3}) contained in a 4-mm ID by 4-mm long epoxy ($C_{40}H_{51}N_2O_7$, initial density 1.185 g cm^{-3}) can (a right circular cylinder) fully open at both ends to allow entry of the laser beams. The can wall thickness was 25 μm. The targets were illuminated with 350 kJ of 351 nm laser light in either 132 beams (Shot 1)

or 112 beams (Shots 2-5). For Shot 1, all 128 of the outer-cone beams were used, 64 beams incident at 44.5^0 and 64 at 50^0 to the can axis, plus the four of the 30^0 beams on which there are backscatter diagnostics On this shot all outer cone beams were overlapped at the laser entrance holes (LEHs), and the 30^0 beams overlapped 1.5 mm outside each LEH.

On Shots 2 through 5, just 84 of the outer-cone beams were used, and these beams were overlapped at a position on the can axis 0.5 mm inside each LEH. Pre-shot simulations had suggested that emissivity would be several percent more with this inward pointing of the outer-cone beams. The simulations also suggested that the emissivity would be insensitive to the exact beam configuration (i.e., how many beams in which beam cones) and would also be insensitive to the inner-cone beam pointing, Accordingly, in Shots 2 through 5 we used 28 of the 32 30^0 beams, overlapped, as in Shot 1, 1.5 mm outside each LEH.

These beam configurations and beam pointings are summarized in Table I.

Table I. Number of beams per LEH and beam pointing for the two different beam configurations of the 2009 NIF Ar/Xe shots

	30^0 beams	44.5^0 beams	50^0 beams	total
NIF Shot1	4 (bottom) 0 (top)	32 32	32 32	132
Pointing*	+1.5	0	0	
NIF Shots2,4,5	12(bottom) 16(top)	16 16	28 24	112
Pointing*	+1.5	-0.5	-0.5	

*distance in mm from LEH: positive is outside LEH, negative is inside LEH

All shots used the same ~5 ns slow-rise pulse, i.e., 1 ns rise to peak power, 4 ns flat-top, 0.2 ns fall to zero. Continuous Phase Plates were used on each beam to produce smooth

elliptical focal spots, with spot radii at the 50% intensity contours of 593 μm x 343 μm for the 30^0 beams, and 824 μm x 590 μm for the 50^0 beams. Thus, there is a non-negligible amount of energy outside the focal spots.

2.1 Simulations

The particular Ar/Xe gas mix was chosen because, for these particular experiments, we wanted significant x-ray output in the 1.5-6 keV x-ray energy range. In this photon energy band are the higher-order Xe M shell (~1.5-2.5 keV), the Ar K-shell (~3 keV), and the Xe L-shell (~4-5.5 keV) transitions. The initial gas fill density was chosen because the modeling simulations show that gas of this density, when illuminated by the 350 kJ from the NIF laser, becomes plasma with a nearly uniform electron density of approximately one-tenth the critical density, i.e., $n_e \sim 10^{21}$ cm^{-3} at the time of peak electron temperature, 1 ns, as shown in Fig. 1a. This electron density is optimum for efficient x-ray conversion. This is because the radiated power is proportional to the square of the electron density [7], so much lower-density plasmas do not radiate as efficiently (and, for a given beam energy, do not get as hot), while plasmas with densities greater than $\sim n_c/4$ have plasma waves that anomalously absorb or scatter the incident laser light [24].

Note also, as shown in Fig. 1b, that after 1 ns the hot plasma is already expanding out the LEHs; by 2 ns only about half of the original volume of the plasma is above $0.1n_c$ electron density. Likewise, as seen in Fig. 2, the plasma reaches a peak temperature on axis of almost 5 keV at 1 ns, when the heating laser pulse first reaches peak power. After 1 ns the plasma begins to cool, but then re-heats as it is compressed on axis by the exploding can, reaching a peak temperature of 6 keV near the end of the laser pulse, at 4.5 ns. For most of the pulse, however, the plasma temperature stays below 5 keV.

NIF Shots 2 through 5 were nominally identical, except that on Shot 3 we had to drop one bundle of eight beams right before the shot, so the total beam energy on Shot 3 was

329 kJ rather than 350 kJ [20]. Nonetheless, both the total x-ray emission at photon energies >1.5 keV and the total emission at photon energies >3 keV scale linearly with total beam energy over this narrow energy range, so the x-ray conversion efficiencies are approximately the same for Shots 2 through 5. The simulated x-ray output for Shot 2 is shown in Fig. 3. In Fig. 3a is the >1.5 keV emitted power history into 4π steradians (the upper curve), out through the can walls (the middle curve), and out the LEHs (the lower curve); in Fig. 3b is the time-integrated emitted spectral energy. The simulation captures the details of the line structure in the Xe M and L shells and the Ar K shell. For this particular gas mix, these three spectral bands have comparable peak spectral emissivities.

2.2 Comparison of simulations with NIF data

Broad-band spectral emission was measured by an absolutely calibrated array of filtered x-ray diodes, the Dante detector [25]. Filter materials and thicknesses were chosen so as to cover the spectral ranges for the expected Ar and Xe emission. The actual Dante configurations we used are described in detail in ref. 20. Of course, Dante measures the time history of the emitted power per steradian in just the angular direction of the detector's position with respect to the target. For the NIF experiments we took measurements with two Dante detectors. Here we compare the simulations to the unfolded data from Dante-1, which is positioned so as to view the target at an angle of 37^0 with respect to the target axis. Thus, Dante-1 sees some of the emission coming from one LEH and some coming through the partially opaque can wall. In unfolding the data, we take the 18 voltage-vs.-time traces from the 18 broad-band-filtered Dante channels, as recorded on high-speed oscilloscopes, and numerically reconstruct the spectral powers incident on the detector in each channel by accounting for the filter and detector response function, the cable attenuations, and the aperture sizes [25, 26, 27].

To compare the simulations with the data, we first post-process the simulation results by solving the radiation transport equation for the particular angular direction to Dante-1

from each emitting element in the simulation to get the spectral powers incident on the detector. Then, we convolve these powers with the detector response functions and cable attenuations to produce 18 simulated voltage-vs.-time traces. Finally, we unfold the simulated Dante data in precisely the same way we unfold the actual data to produce the simulated output in each of the photon energy regions of interest.

The results of this process for the emitted power histories in two photon energy bands are shown in Fig. 4 for Shot 1 and Shot 2; results for the time-integrated emitted spectral energies for the same two shots are shown in Fig. 5.

There are several things to note from this comparison. First, we note that the total >1.5 keV emission from Shot 2 is greater than that from Shot 1, just as predicted in the simulations. This is largely due to the different outer-cone beam pointing; the more-inward pointing on Shot 2 couples more of the beam energy to the plasma. We also find that the simulations provide a good match to the measured total >1.5 keV emission on both shots. The >3 keV emission on both shots, however, is under-predicted in the simulations. In Fig. 5 we note that the simulation over-predicts emission in the Xe M band, and under-predicts emission in the Ar K band and Xe L band. It is not clear if these discrepancies are artifacts of the data unfold technique or a result of not having enough ionization levels included in the simulations. A high-resolution spectrometer which we hope to field on future shots will help to resolve these discrepancies.

2.3 Sensitivities

For a given beam cone configuration, we find very little sensitivity of x-ray emission to pointing of the inner-cone beams. This is perhaps not surprising, since the actual focal spots have some non-negligible depth along the ray axis, so changing the pointing by distances comparable to the focal depth (on the order of a couple of mm) does not change the beam intensity.

It is a different story, however, for the outer-cone beams. These beams are entering the gas at such a steep angle that the path length through the gas, and thus the amount of plasma that is directly heated by the beams, is quite sensitive to the pointing of the beams with respect to the LEH. We find that moving the pointing of the outer-cone beams inward from the LEH (more toward can center) by a mere 0.5 mm increases the >1.5 keV emission by ~20%; for NIF Shot 2, with the inward pointing, the simulated >1.5 keV x-ray conversion efficiency is 19.7%, whereas for NIF Shot 1, with pointing at the LEH, it is 16.6%.

For constant beam pointings and constant total beam energy, we also find very little change in the simulated x-ray conversion efficiency with variations in the beam configuration, i.e., the number of beams in each beam cone. Thus, the ~20% greater >1.5 keV emission for NIF Shot 2 than for NIF Shot 1, both simulated and measured, is due entirely to the inward pointing of the outer-cone beams and not to the different beam configuration.

For a given total beam energy, beam configuration, gas mix, and initial gas pressure, increases in the can length give somewhat less uniform heating of the gas volume, with a modest decrease in the x-ray conversion efficiency that is dependent on the gas mix and initial pressure. For example, we find that for a pure Kr gas with initial fill pressure 1.2 atm illuminated by 100 TW of NIF, the simulated x-ray conversion efficiency for the Kr L shell (photon energies >1.5 keV) is 19.6% for a 4-mm-long can and 18.7% for a 7-mm-long can; the corresponding numbers for the Kr K shell (photon energies >12.5 keV) are 0.6% and 0.5%.

There is a complicated dependence of x-ray conversion efficiency on the initial gas fill pressure because the fill pressure has a large effect on the can hydrodynamics. If the pressure is too low, implosion of the can walls unhindered by back pressure from the gas leads to a closing of the laser entrance holes, inability of the laser beams to get in and properly heat the gas volume, and a large drop in the x-ray conversion efficiency. Likewise, too high a gas pressure can lead to over-dense regions that prevent supersonic

heat propagation and result in inefficient heating. Simulations suggest that it is best not to go below about 80% or above about 120% of the nominal fill pressure.

The targets are filled after insertion into the target chamber, and a pressure transducer monitors the fill pressure right up to shot time. Thus, if the target springs a leak before the shot, we would know about it and can scrub the shot.

3. Scaling with Power and Atomic Number

In Fig. 6 we see that the simulated Xe L-shell x-ray conversion efficiency increases modestly with laser power, and levels off at ~150 TW. These simulations were done for 1.0 atm of pure Xe gas, and for two different beam configurations and two different pulse shapes. The slow-rise pulse shape rises from zero to peak power over 1 ns, like for the NIF Ar/Xe shots discussed in the previous section. The fast-rise pulse shape rises from zero to peak power in 0.2 ns. As discussed in Section 2.3, x-ray conversion efficiency is insensitive to beam configuration. Thus, the red and blue curves in Fig. 6 overlay each other. The sensitivity to pulse shape at the higher powers, shown in Fig. 6, comes about only because, for a given peak power and pulse duration, there is less total beam energy in the slow-rise pulse than in the same-power fast-rise pulse. Thus, the plasma does not get as hot with the slow-rise pulse, and even decreases as the power increases above 150 TW.

The general behavior of the x-ray conversion efficiency leveling out above about 150 TW is not unique to Xe. We found the same behavior for the Kr K-shell. We can begin to understand this behavior when we consider that efficient conversion of laser energy to multi-kilovolt x-rays depends upon supersonic heating of the plasma, and remember that the ionization/heating front travels at a velocity ~1 mm/ns in the low-density material. As the plasma heats, however, the adiabatic sound speed increases. As we see in Fig. 7, supersonic heating is limited to plasmas with electron temperature less than about 10 keV, with this limit slightly higher in higher-Z plasmas. The velocity of

the heating wave is about a thousand times faster than the sonic velocity in the cold material, but only about twice the sonic velocity in the ~5 keV NIF Ar/Xe plasma.

Furthermore, plasma temperatures are clamped by adiabatic expansion cooling as the hot plasma jets out the LEHs. Cooling is further enhanced by electron thermal conduction in the steep temperature gradient of the expanding plasma. These physical processes are illustrated in Fig. 8. In this figure are shown the maximum expansion velocity of the plasma on axis (the black curves) and the maximum electron temperature on axis (the red curves) for the NIF Ar/Xe shots (the solid curves) and the Omega Ge-doped aerogel shots (the dashed curves). Plasma expands adiabatically into vacuum at a velocity about twice the sound velocity. For both the Omega shots and the NIF shots, the expansion velocity already approaches the velocity of the heating wave during the time the heating pulse is at peak power. The NIF targets reach first peak temperature when the heating pulse reaches peak power, ~1 ns. Then, the plasma cools via adiabatic expansion and thermal conduction. The plasma reheats near the end of the pulse because of compression on axis by the stagnating can. After the heating pulse turns off, the plasma cools very rapidly, much faster in the ~5 keV NIF plasma than in the ~2.5 keV Omega plasma. The cooling processes thus keep the bulk of the NIF plasma at 4-5 keV, nearly independent of the beam power. This is why there is little improvement in x-ray conversion efficiency for laser powers above about 150 TW.

In practice, the laser power is limited to <125 TW because of beam back-scatter from plasma instabilities. In Stimulated Brillouin Scattering (SBS), photons scatter from ion acoustic waves in the plasma, with a scattered intensity gain $I_{SBS}/I_0 \sim \exp(G_{SBS})$. We computed G_{SBS} from the plasma code LIP [28], using plasma parameters along the beam path taken from the Lasnex simulation. Results of these LIP simulations for a NIF Kr target are shown in Fig. 9, along with the Kr L-shell and K-shell x-ray conversion efficiencies as a function of total beam power. Note that the Kr L-shell conversion efficiency is approximately constant with beam power. The Kr K-shell conversion efficiency rises modestly with laser power; it is about 50% greater at 220 TW than what it is at 100 TW. Note, however, that the SBS gain exponent rises very steeply with

beam power. The initial plasma turbulence noise level is unknown, but is assumed to be ~10^{-9}-10^{-8}. Thus, for tolerable SBS, G_{SBS} must remain less than 18-21. From Fig. 9 this restraint on SBS gain limits us to beam powers less than about 125 TW.

There are a couple of caveats to this result. The LIP simulations show that the SBS back scatter is much greater than the Stimulated Raman Scatter (SRS, scattering of the electromagnetic waves from longitudinal electron plasma waves), and that it is the SBS on the outer beam cones that dominates. The back scatter measurements made on the NIF Ar/Xe shots, on the other hand, show that there was more SRS back scatter than SBS. The measured SBS was negligible, ~0.2%, on all beam cones and on all these ~70 TW shots, consistent with simulations. On the other hand, the measured SRS on the outer beam cones on all shots, ~0.7%-3.5%, was much more than calculated, and was negligible on the inner beam cones on all shots except Shot 1. Back scatter on the outer beam cones is strongly influenced by beam interaction with plasma blowing off the end of the cans. This is the region in the Lasnex simulation that is most affected by inaccuracies introduced by the rezoning across region boundaries. Further, the LIP simulation does not account for either damping of SBS by the SRS, or cross-beam energy-transfer effects. Indeed, the much higher SRS measured on Shot 1 on both the inner and outer cones is consistent with the much more beam overlap in this shot because of the beam configuration and pointing, i.e., more outer cone beams at higher overlap intensity than in Shots 2 through 5. It was recently discovered [29] that there is a lot of interaction in the beam overlap region in ignition hohlraum experiments, so it is not surprising that we cannot predict the backscatter levels without including some multi-beam effects. Thus, we cannot necessarily conclude that the beam power limit imposed by the restraint on SBS back scatter is a real limit. This remains an open question.

Nonetheless, for purposes of estimating the scaling of K-shell x-ray conversion efficiency with atomic number Z, we simulated a nominal optimum pure Zn target, a nominal optimum pure Kr target, and a nominal optimum Fe_2O_3 foam target, each illuminated by 100 TW of NIF beams. K-shell x-ray conversion efficiencies for these

targets are shown in Figure 10, along with the x-ray conversion efficiencies measured from almost all past Omega shots on under-dense targets. The Omega, Nova and Gekko data were taken from references 7 through 14, 16, 17, and 30.

The general scaling of x-ray conversion efficiency with Z is the same for NIF as for the lower-power lasers, but the higher energy and power available with NIF provides modestly higher x-ray conversion efficiency, by about 50%, for a given Z. Of course, the much higher beam energy means that much more total K-shell emission can be achieved.

4. Discussion and Summary

In summary, we have incorporated a modern DCA non-LTE atomic model into a 2D radiation-hydrodynamics code, and benchmarked the new model with data from very low-density Ge-doped silica aerogel foam targets on Omega. We then used the same computational model to design Ar/Xe gas targets for NIF. Post-shot simulations of the actual NIF Ar/Xe shots that were conducted in October and November of 2009 were completed, along with simulated voltage versus time traces as would be seen from the Dante broad-band filtered x-ray diode array. These simulations were compared with the measurements taken on the NIF shots.

We find good agreement between simulated and measured emissions summed over all photon energies, and at photon energies >1.5 keV. The simulations, however, under-predict the >3 keV emission.

Further, we find that adiabatic expansion cooling and electron thermal conduction keep the plasma temperatures in NIF targets at ~5 keV, nearly independent of total beam power, which limits the peak x-ray conversion efficiency that can be achieved at high power at NIF. Simulations also suggest that Stimulated Brillouin Scattering limits the practical peak power to less than about 125 TW. This power limit suggests that NIF can make x-ray sources with only modestly higher x-ray conversion efficiency than

what has been done at lower power. For optimum NIF targets, i.e., those for which the electron density is between about 10% and 15% of the critical density, we might expect 50% higher K-shell x-ray conversion efficiency than what has been achieved on Omega. The real advantage of NIF, however, is in making x-ray sources that are much larger, more uniform, of much longer duration, and much brighter than ever done before.

Acknowledgements

This work was performed under the auspices of the US Department of Energy by Lawrence Livermore National Laboratory (LLNL) under contract No. DE-AC52-07NA27344, with some support received from the US Defense Threat Reduction Agency under the IACRO 09-45501, "Evaluation of Lasers for X-Ray Production on NIF". One of the authors (JDC) would like to thank Judy Harte of LLNL for help with the Lasnex simulations, Denise Hinkel of LLNL for help with the LIP simulations, and Mordy Rosen of LLNL for useful discussions.

References

[1] J. Denavit and D. W. Phillion, Phys. Plasmas **1**, 1971 (1994).

[2] C. A. Haynam *et al*., Appl. Opt. **46**, 3276 (2007).

[3] J. D. Colvin, K. B. Fournier, M. J. May, and H. A. Scott, Phys. Plasmas **17**, 073111 (2010).

[4] C. Constantin, C. A. Back, K. B. Fournier, G. Gregori, O. L. Landen, S. H. Glenzer, E. L. Dewald, and M. C. Miller, Phys. Plasmas **12**, 063104 (2005).

[5] M. Tanabe, H. Nishimura, S. Fujioka, K. Nagai, A. Iwamae, N. Ohnishi, K. B. Fournier, F. Girard, M. Primout, B. Villette, M. Tobin, and K. Mima, Proc. Conf. Int. Fusion Sciences and Applications (IFSA2007), J. Phys.: Conf. Series **112**, 022076 (2008).

[6] M. Tanabe, H. Nishimura, N. Ohnishi, K. B. Fournier, S. Fujioka, A. Iwamae, S. B. Hansen, K. Nagai, F. Girard, M. Primout, B. Villette, D. Brebion, and K. Mima, High Energy Density Phys. **6**, 89-94 (2010).

[7] C. A. Back, J. Grun, C. Decker, L. J. Suter, J. Davis, O. L. Landen, R. Wallace, W. W. Hsing, J. M. Laming, U. Feldman, M. C. Miller, and C. Wuest, Phys. Rev. Lett. **87**, 275003 (2001).

[8] C. A. Back, J. Davis, J. Grun, L. J. Suter, O. L. Landen, W. W. Hsing, and M. C. Miller, Phys. Plasmas **10**, 2047 (2003).

[9] K. B. Fournier, C. Constantin, C. A. Back, L. Suter, H.-K. Chung, M. C. Miller, D. H. Froula, G. Gregori, S. H. Glenzer, E. L. Dewald, and O. L. Landen, JQSRT **99**, 186 (2006).

[10] M. Tanabe, H. Nishimura, S. Fujioaka, K. Nagai, M. Yamamoto, Z-Z. Gu, C. Pan, F. Girard, M. Primout, B. Villette, D. Brebion, K. Fournier, A. Fujishima, and K. Mima, Appl. Phys. Lett. **93**, 051505 (2008).

[11] F. Girard, J. P. Jadaud, M. Naudy, B. Villette, D. Babonneau, and M. Primout, Phys. Plasmas **12**, 092705 (2005).

[12] D. Babonneau, M. Primout, F. Girard, J.-P. Jadaud, M. Naudy, B. Villette, S. Depierreux, C. Blancard, G. Faussurier, K. B. Fournier, L. Suter, R. Kauffman, S. Glenzer, M. C. Miller, J. Grun, and J. Davis, Phys. Plasmas **15**, 092702 (2008).

[13] M. Primout, L. Jacquet, D. Babonneau, F. Girard, B. Villette, J.-P. Jadaud, M. Naudy, Ph. Stemmler, and J. L. Ulmer, J. Phys.: Conf. Ser. **112**, 042051 (2008).

[14] F. Girard, M. Primout, B. Villette, Ph. Stemmler, L. Jacquet, D. Babonneau, and K. B. Fournier, Phys. Plasmas **16**, 052704 (2009).

[15] B. J. Clapsaddle, D. W. Sprehn, A. E. Gash, J. H. Satcher, Jr., and R. L. Simpson, J. Non-Crystalline Solids **350**, 173 (2004).

[16] K. B. Fournier, C. Constantin, J. Poco, M. C. Miller, C. A. Back, L. J. Suter, J. Satcher, J. Davis, and J. Grun, Phys. Rev. Lett. **92**, 165005 (2004).

[17] K. B. Fournier, J. H. Satcher, M. J. May, J. F. Poco, C. M. Sorce, J. D. Colvin, S. B. Hansen, S. A. MacLaren, S. J. Moon, J. F. Davis, F. Girard, B. Villette, M. Primout, D. Babonneau, C. A. Coverdale, and D. E. Beutler, Phys. Plasmas **16**, 052703 (2009).

[18] J. Biener, T. F. Baumann, Y. Wang, E. J. Nelson, S. O. Kucheyev, A. V. Hamza, M. Kemell, M. Ritala, and M. Leskelä, "Ruthenium/aerogel nanocomposites via atomic layer deposition", *Nanotechnology* **18**, 055303 (2007).

[19] J. D. Colvin and T. E. Felter, Bull. A.P.S. **48**, 288 (2003).

[20] K. B. Fournier, M. J. May, J. D. Colvin, J. O. Kane, M. Schneider, E. Dewald, C. A. Thomas, S. Compton, R. E. Marrs, J. Moody, E. Bond, P. Michel, J. H. Fisher, C. D. Newlander, and J. F. Davis, Phys. Plasmas **17**, 082701 (2010).

[21] H. A. Scott and S. B. Hansen, High Energy Density Phys. **6**, 39-47 (2010).

[22] L. Spitzer, *Physics of Fully Ionized Gases* (Wiley, New York, N. Y., 1962).

[23] G. B. Zimmerman and W. L. Kruer, Comments Plasma Phys. Control. Fusion **2**, 51 (1975).

[24] D. W. Forslund, J. M. Kindel, and E. L. Lindman, Phys. Fluids **18**, 1002 (1975).

[25] E. L. Dewald, K. M. Campbell, R. E. Turner, J. P. Holder, O. L. Landen, S. H. Glenzer, R. L. Kauffman, L. J. Suter, M. Landon, M. Rhodes, and D. Lee, Rev. Sci. Instr. **75**, 3759 (2004).

[26] C. Sorce, J. Schein, F. Weber, K. Widmann, K. Campbell, E. Dewald, R. Turner, O. Landen, K. Jacoby, P. Torres, and D. Pellinen, Rev. Sci. Instr. **77**, 10E518 (2006).

[27] A. Seifter and G. A. Kyrala, Rev. Sci. Instr. **79**, 10F323 (2008).

[28] D. J. Strozzi, E. A. Williams, D. E. Hinkel, D. H. Froula, R. A. London, and D. A. Callahan, Phys. Plasmas **15**, 102703 (2008).

[29] D. E. Hinkel, Bull. A.P.S **55**, 21 (2010).

[30] J. Workman and G. A. Kyrala, Rev. Sci. Instr. **72**, 678 (2001).

Figure Captions

Fig. 1 (Color). Electron density contours a) at 1.0 ns and b) at 2.0 ns for the baseline Ar/Xe NIF target as simulated with the DCA non-LTE atomic model and Spitzer-Harm electron thermal conductivities. The closed red curve shows the outline of the epoxy can that contains the Ar/Xe plasma. Only one quadrant is shown; the contours have rotational symmetry around the can axis (radial coordinate r=0) and reflection symmetry in the mid-plane (the plane at axial coordinate z=0). The laser beams enter from the right.

Fig. 2. Maximum electron temperature on the can axis as a function of time for the baseline Ar/Xe NIF target as simulated with the DCA non-LTE atomic model and Spitzer-Harm electron thermal conductivities.

Fig. 3. For NIF Shot 2, a) x-ray emitted power as a function of time in photon energies of 1.5-5.5 keV and b) time-integrated up to 2.5 ns (dotted curve), 5.0 ns (dash-dot curve), 7.5 ns (dashed curve), and 10.0 ns (solid curve) x-ray emitted spectral energy as a function of photon energy, as simulated with the DCA non-LTE atomic model and Spitzer-Harm electron thermal conductivities.

Fig. 4 (Color). X-ray emitted power as a function of time in several photon energy bands as seen from the Dante-1 detector, as simulated (blue curves) and as measured (red curves), for a) NIF Shot 1 and b) NIF Shot 2.

Fig. 5 (Color). Time-integrated x-ray emitted spectral energy as a function of photon energy as seen from the Dante-1 detector, as simulated (blue curves) and as measured (red curves), for a) NIF Shot 1 and b) NIF Shot 2.

Fig. 6 (Color). Simulated x-ray conversion efficiency in photon energies >1.5 keV as a function of total laser power for a NIF target of pure Xe with an initial fill pressure of

1.0 atm contained in a 4-mm x 4-mm epoxy can. Simulations were done for two different beam configurations and two different pulse shapes.

Fig. 7. Adiabatic sound speed as a function of electron temperature in a silica plasma (solid curve) and in a Kr plasma (dashed curve).

Fig. 8 (Color). Maximum plasma expansion velocity (black curves) and maximum electron temperature (red curves) on axis as a function of time, as simulated for the NIF Ar/Xe target (solid curves) and for the Omega Ge-doped silica aerogel target (dashed curves).

Fig. 9 (Color). Kr L-shell x-ray conversion efficiency (%, blue curve), Kr K-shell x-ray conversion efficiency (%x50, green curve), and SBS gain exponent (red curve) as a function of total laser power. All simulations were done for a pure Kr target illuminated by 500 kJ in 160 NIF beams with the fast-rise pulse.

Fig. 10 (Color). X-ray conversion efficiency as a function of x-ray energy for past Omega shots, for the Ar/Xe NIF shots, and as predicted for "optimum" NIF targets of Fe, Zn and Kr.

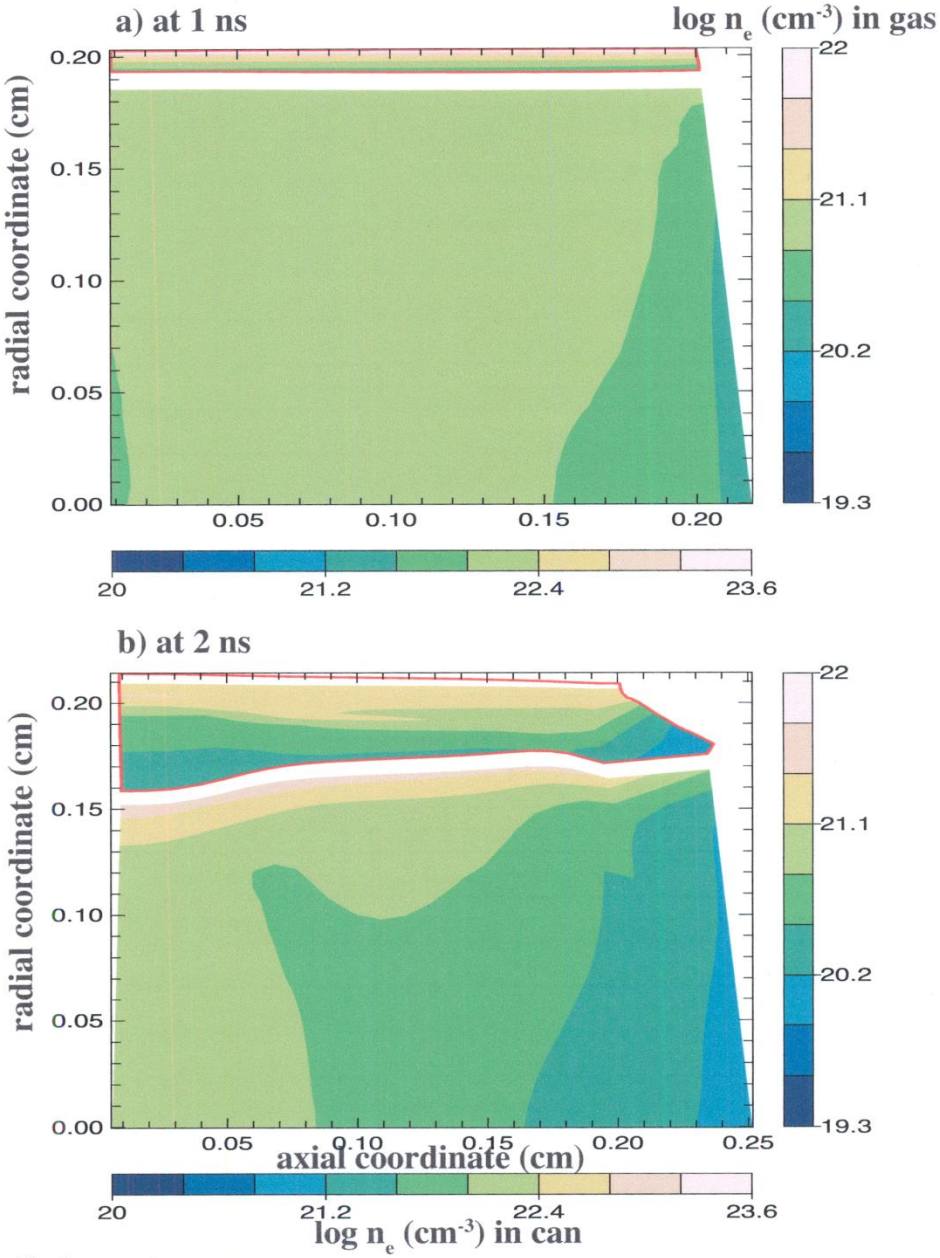
a) at 1 ns
log n_e (cm^-3) in gas
radial coordinate (cm)
0.20
0.15
0.10
0.05
0.00
0.05
0.10
0.15
0.20
22
21.1
20.2
19.3
20
21.2
22.4
23.6
b) at 2 ns
radial coordinate (cm)
0.25
axial coordinate (cm)
log n_e (cm^-3) in can

Colvin_Fig. 1

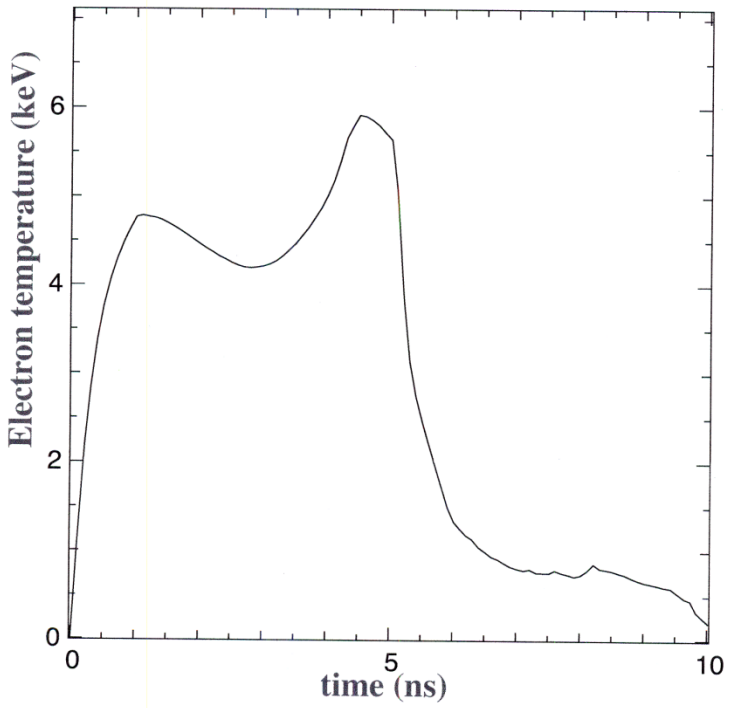

Colvin_Fig. 2

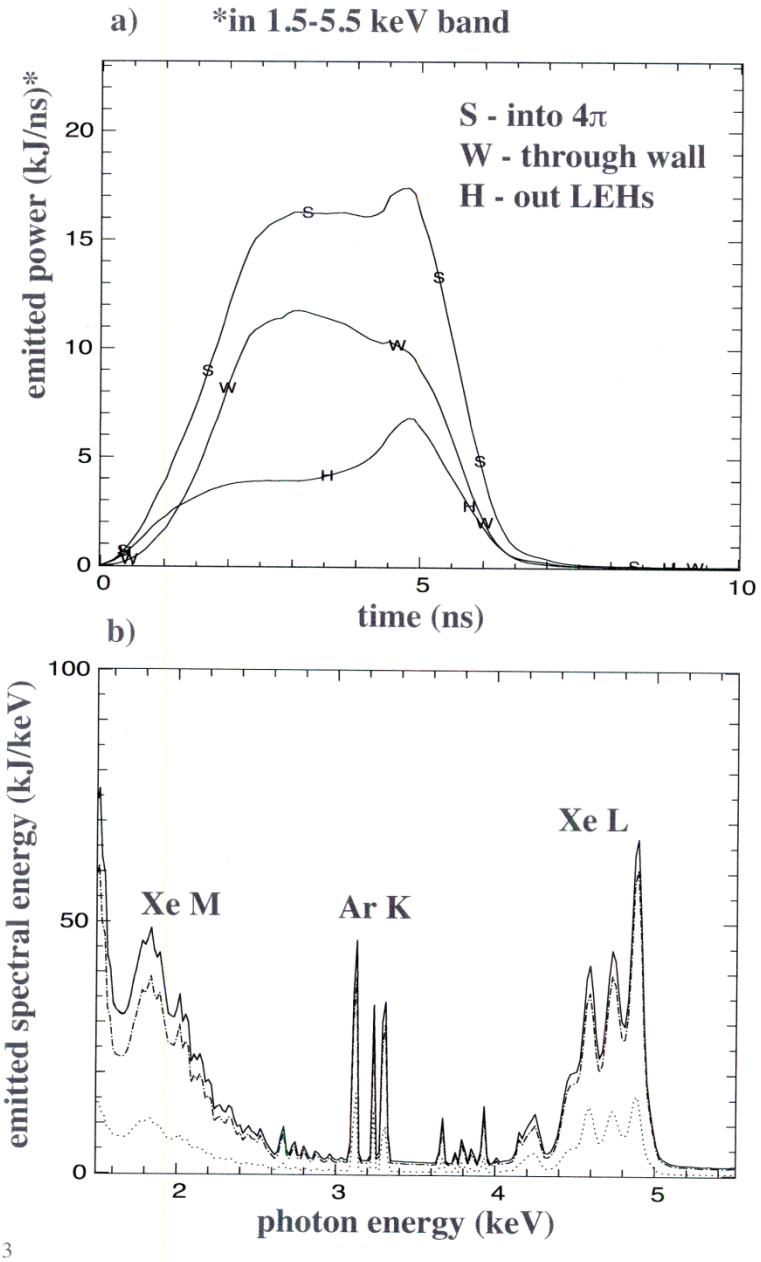
a)
*in 1.5-5.5 keV band
emitted power (kJ/ns)*
S - into 4π
W - through wall
H - out LEHs
time (ns)
b)
emitted spectral energy (kJ/keV)
Xe M
Ar K
Xe L
photon energy (keV)

Colvin_Fig. 3

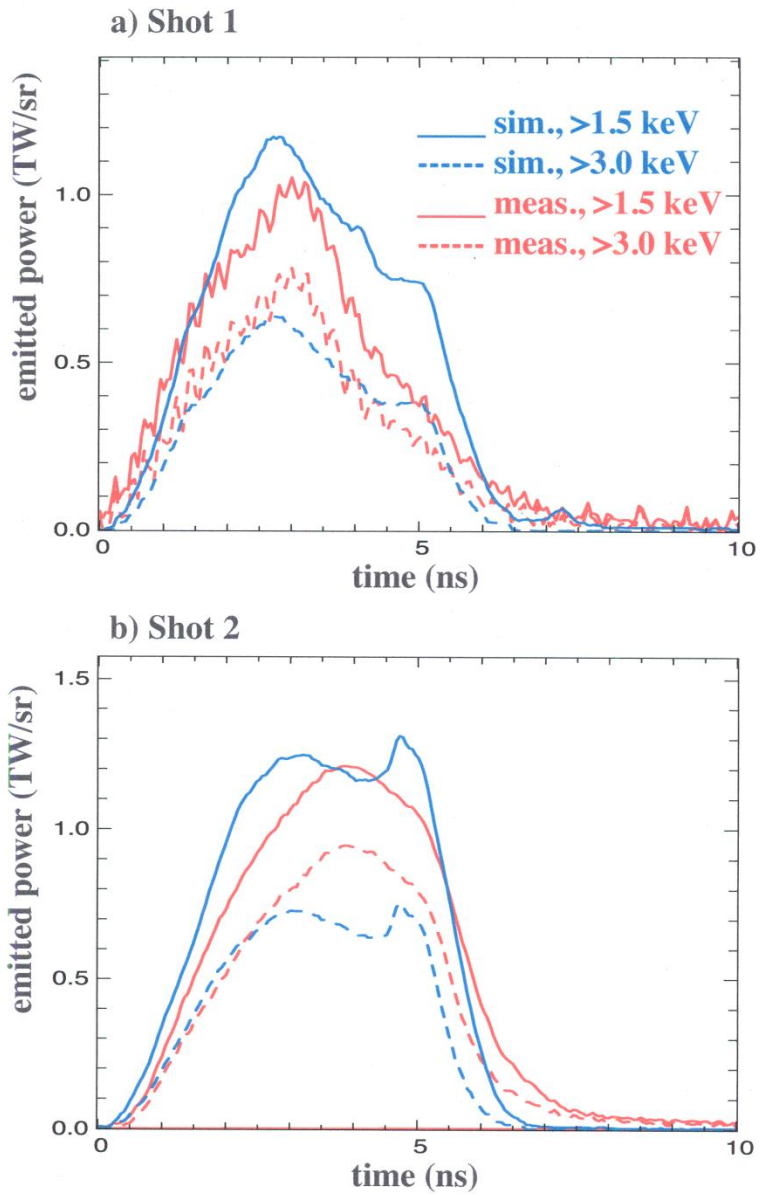
a) Shot 1
emitted power (TW/sr)
1.0
0.5
0.0
0
5
10
time (ns)
sim., >1.5 keV
sim., >3.0 keV
meas., >1.5 keV
meas., >3.0 keV
b) Shot 2
emitted power (TW/sr)
1.5
1.0
0.5
0.0
0
5
10
time (ns)

Colvin_Fig. 4

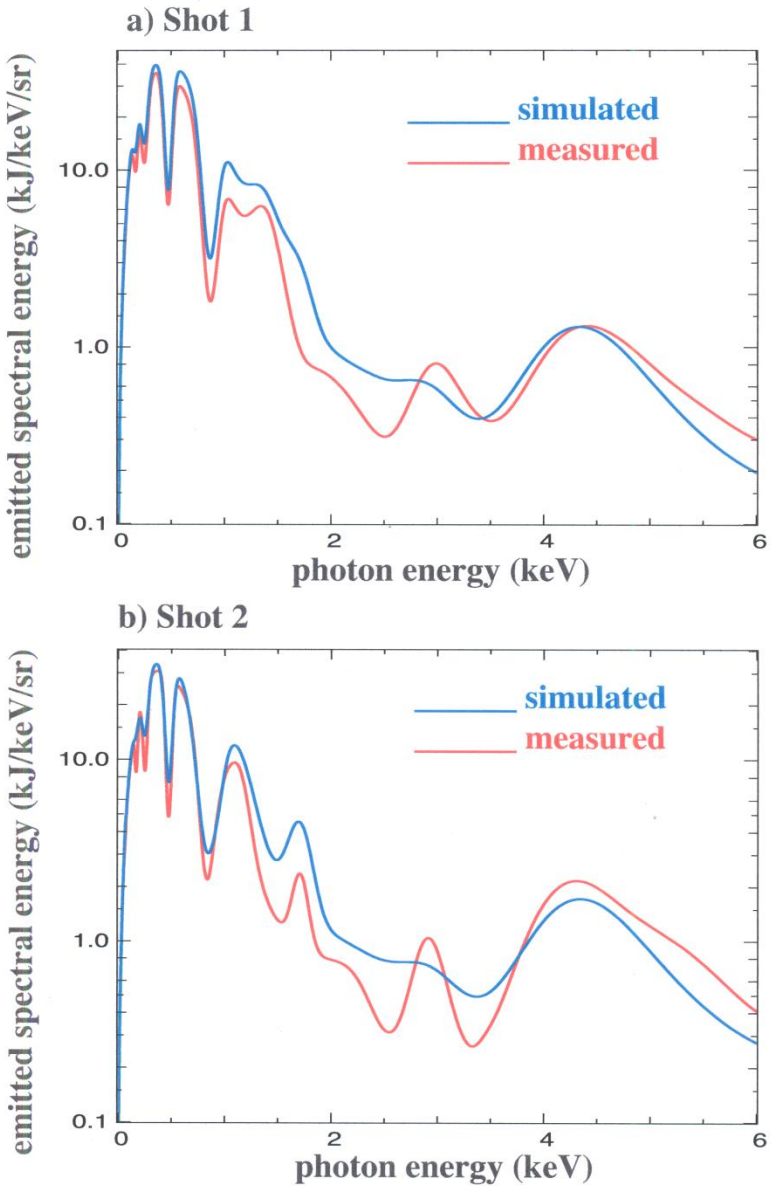
a) Shot 1
emitted spectral energy (kJ/keV/sr)
simulated
measured
10.0
1.0
0.1
0
2
4
6
photon energy (keV)
b) Shot 2
emitted spectral energy (kJ/keV/sr)
simulated
measured
10.0
1.0
0.1
0
2
4
6
photon energy (keV)

Colvin_Fig. 5

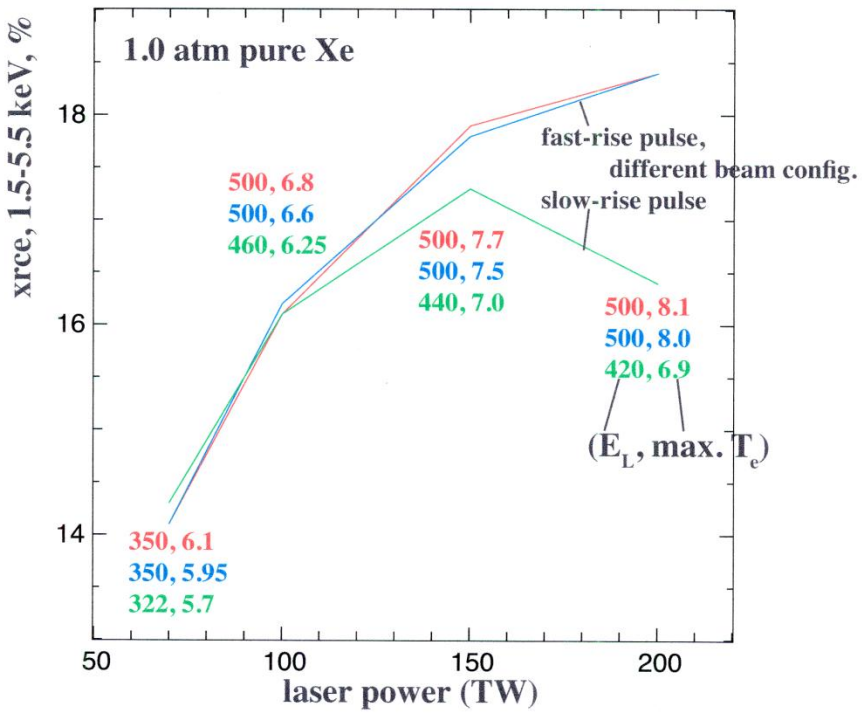
1.0 atm pure Xe
xrce, 1.5-5.5 keV, %
18
16
14
50
100
150
200
laser power (TW)
500, 6.8
500, 6.6
460, 6.25
500, 7.7
500, 7.5
440, 7.0
fast-rise pulse,
different beam config.
slow-rise pulse
500, 8.1
500, 8.0
420, 6.9
(E_L, max. T_e)
350, 6.1
350, 5.95
322, 5.7

Colvin_Fig. 6

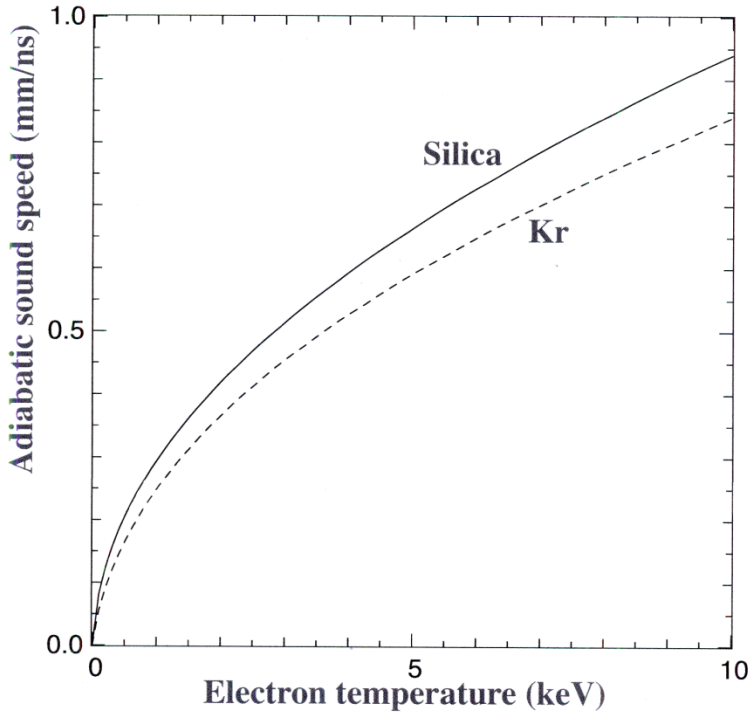
Adiabatic sound speed (mm/ns)
1.0
0.5
0.0
0
5
10
Electron temperature (keV)
Silica
Kr

Colvin_Fig. 7

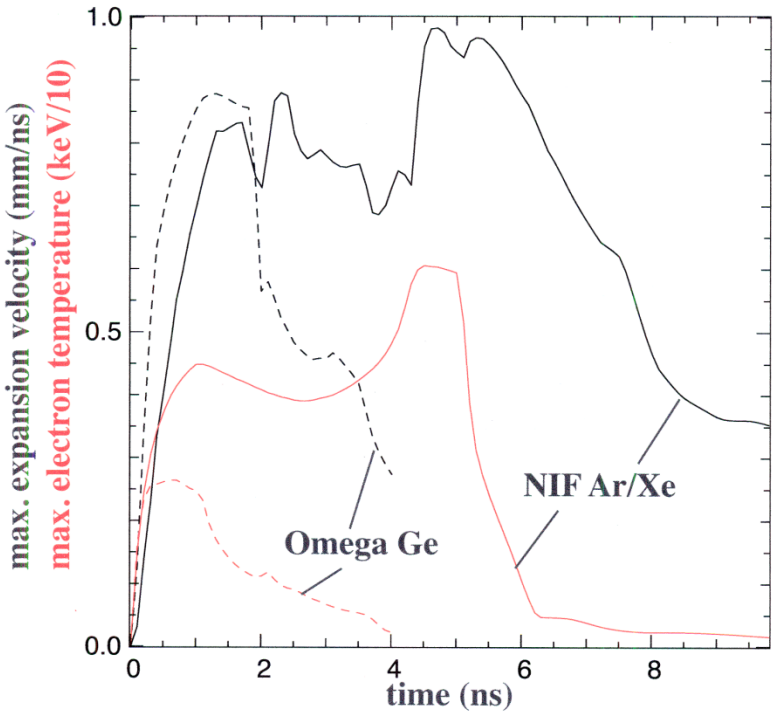
1.0
0.5
0.0
0
2
4
6
8
time (ns)
max. expansion velocity (mm/ns)
max. electron temperature (keV/10)
NIF Ar/Xe
Omega Ge

Colvin_Fig. 8

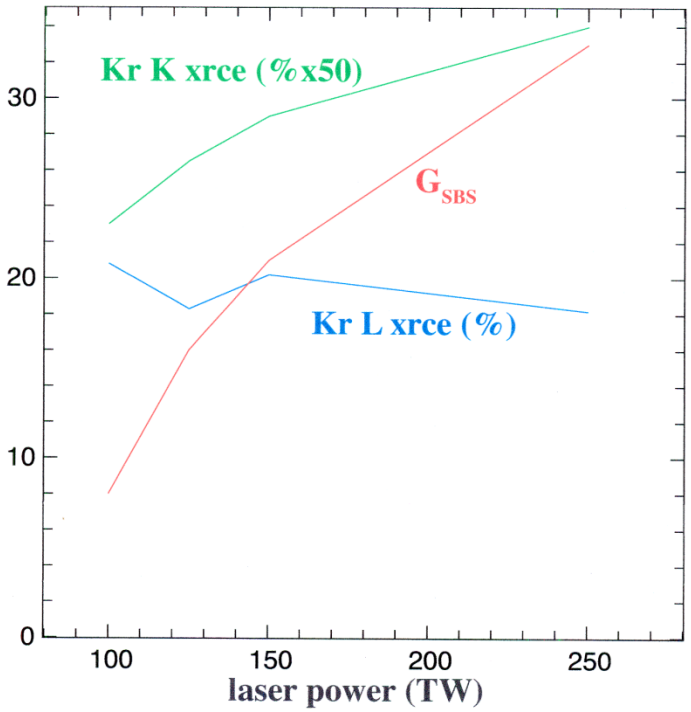
Kr K xrce (%x50)
G SBS
Kr L xrce (%)
30
20
10
0
100
150
200
250
laser power (TW)

Colvin_Fig. 9

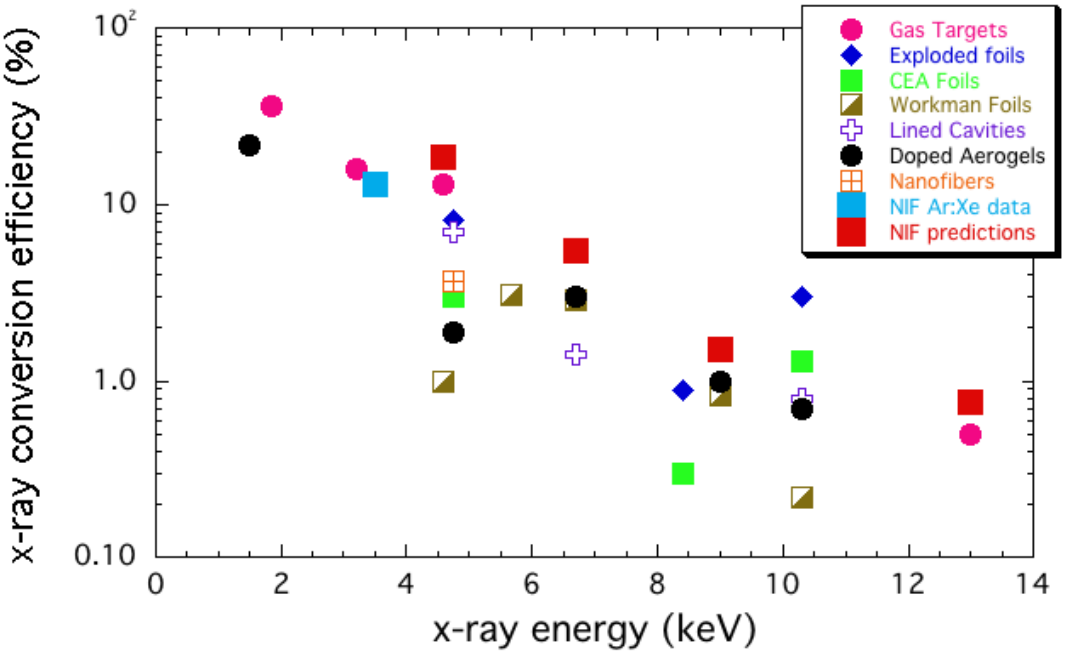

Colvin_Fig.10